**Original Article**

# Depth-resolved numerical model of dam break mud flows with Herschel-Bulkley rheology

**TANG Jin-bo[1,2]** http://orcid.org/0000-0002-7192-1224; e-mail: jinbotang@imde.ac.cn

**LIN Peng-zhi[1]\*** https://orcid.org/0000-0002-4437-5571; ✉e-mail: cvelinpz@126.com

**CUI Peng[2,3]\*** https://orcid.org/0000-0002-3973-5966; ✉e-mail: pengcui@imde.ac.cn

*\*Corresponding author*

*1 State Key Laboratory of Hydraulics and Mountain River Engineering, Sichuan University, Chengdu 610065, China*

*2 Key Laboratory of Mountain Hazards and Earth Surface Processes, Chinese Academy of Sciences, Institute of Mountain Hazards and Environment, Chinese Academy of Sciences and Ministry of Water Conservancy, Chengdu 610041, China*

*3 Institute of Geographic Sciences and Natural Resources Research, Chinese Academy of Sciences, Beijing 100101, China*

**Citation:** Tang JB, Lin PZ, Cui P (2022) Depth-resolved numerical model of dam break mud flows with Herschel-Bulkley rheology. Journal of Mountain Science 19(4). https://doi.org/10.1007/s11629-021-7218-0

**Abstract:** Mud flows are common phenomena in mountainous areas, which can threaten human safety and cause property losses under certain extreme circumstances. Studying the dynamic characteristics of mud flows, especially in the vertical direction, is helpful for risk reduction and hazard mitigation. In this study, a 2D depth-resolved numerical model based on Herschel-Bulkley rheology was developed to study the vertical structures of unsteady mud flows with a free-surface. The numerical model was solved by the projection method, and the free surface of mud flows was captured through the VOF method. To fully validate this new model, a series of laboratory experiments involving dam break mud flows were conducted, and the mud flow heights, bottom pressures and envelopes of mud residuum were measured. The numerical model proposed in this study was first validated by the steady-state solution for uniform flows of Herschel-Bulkley fluid on an inclined plane. Additionally, the simulated and measured mud flow heights, bottom pressures at different $x$ locations and envelopes with different bed slopes showed good agreement. Furthermore, the numerical results for a Herschel-Bulkley fluid dam break flow were used to validate the proposed model, which further revealed good agreements. After that, the scenarios in which mud flows impact on a structure were numerically studied, and the vertical profiles of the front velocity and impact pressure on the structure were analyzed and discussed. The results show that a plug layer was formed in the mud flow under unsteady and nonuniform flow conditions, and the impact pressure on the structure was dominated by the dynamic pressure. In addition, the vertical position with the maximum impact pressure acting on the structure was not at the bottom or the surface of the mud flows, and the normalized vertical position rose as the yield stress and consistency coefficient increase for Herschel-Bulkley fluids.

**Keywords:** Mud flows; Herschel-Bulkley rheology; Depth-resolved model; Numerical simulation; Vertical profiles

## 1 Introduction

Mud flows, which consist of highly concentrated mixtures of water and granular materials with a wide

range of grain sizes, are rapid and unsteady geomorphological flows driven by gravity (Iverson 1997; Cui et al. 2005; Ancey 2006). With the widespread development of urbanization, due to the high mobility of mudflows and the large volumes of sediment that they can mobilize, transport and deposit, mud flows pose serious threats to human lives and the safety of property (Zou et al. 2019). Therefore, the development of a reliable method to predict the potential danger of mud flows has become a critical and attractive research topic in recent years (Takahashi 2014).

Rheological experiments involving mud samples have demonstrated the existence of the shear thinning phenomenon, which refers to the decreasing tendency of the apparent viscosity of mud with an increase in the shear rate (Major et al. 1992; Liu et al. 1994; Coussot 1997; Ancey 2006; Wang et al. 2014). These rheological models have been widely used to simulate the propagation of mud flows (Johnson et al. 1970; Chen 1986; Ancey 2006). For example, the depth-averaged method, which removes the information along the depth-direction to reduce the computational cost, has been used to the numerically simulated mud flows in the hazard areas of real catchments (O'Brien 1993; Liu et al. 2006; Fan et al. 2018). The pressure in the depth-averaged method was typically assumed to be approximately hydrostatic (Iverson et al. 2014; Chen et al. 2018). Many efforts have been made to consider the effects of non-hydrostatic in depth-averaged models (Castro-Orgaz et al. 2015, Delgado-Sánchez et al. 2020, and Zhang et al. 2021a, 2021b), however, the vertical velocity profiles of mud flows have not been reported. Additionally, the shear rate used in these depth-averaged models has been assumed to be a ratio of the averaged velocity to the flow depth and the corresponding rheological models have been determined on the basis of flow profiles within the steady and uniform flow regime.

The vertical profiles of velocity and pressure during the motion of mud flows are crucial for understanding the interactions between mud flows and structures, such as the check dams and infrastructures (Bartelt et al. 2006; Kaitna et al. 2014; Leonardi et al. 2016; Liu et al. 2019). However, previous studies have typically obtained vertical profiles of the velocity and pressure for steady and uniform flows (Huang et al. 1998; Mei et al. 2001; Takahashi 2014; Kaitna et al. 2014), which cannot realistically approximate natural mud flows.

In contrast, dam break flows are typically regarded as unsteady and nonuniform free-surface flows, accordingly, many laboratory experiments have been conducted to understand the flow characteristics under unsteady and nonuniform conditions and to validate numerical models (Wang et al. 2000; Ancey et al. 2008; Lin et al. 2011; Cozzolino et al. 2017). Dam break mudflows are more sophisticated than pure water dam break flows because the former flows exhibit non-Newtonian rheology (Coussot 1997). Some researchers have studied dam break mud flows based on depth-averaged models, and have reported the longitudinal profiles of the simulated results (Huang et al. 1997; Huang et al.1998; Nagl et al.2020). Nevertheless, numerical models have not been utilized to present the vertical profiles of velocity and pressure under unsteady and nonuniform free-surface flows, mainly because reliable measured vertical profiles of velocity and pressure have not been available to validate the models owing to the opaqueness of mud flows. Moreover, although some velocity probes have been used to measure the vertical velocity profiles of mud flows under steady and uniform conditions (Louge et al. 1996; Tiefenbacher et al. 2004; Kaitna et al. 2014), such flows could be disturbed by intrusive probes, and thus the measured data might deviate from the truth.

Additionally, some researchers have conducted numerical simulations to study the evolution of mud flows by solving the Navier–Stokes equations. Jing et al. (2018) numerically investigated dam break mud flows on an inclined flume and discussed the effects of rheology on deposit morphology. They found that a higher viscosity could induce wider lateral spreading of the deposit and that a lower yield stress could result in longer deposits. Li et al. (2018) studied the front velocity and surface evolution of dam break mud flows on a horizontal plane based on the OpenFOAM software. They reported that the slope of the mudflow surface decreased in the longitudinal direction and ultimately reached an equilibrium state. However, these models were not adequately validated due to a lack of reliable experimental data, and little attention has been paid to the vertical profiles of the dynamic characteristics under an unsteady state.

In this study, a new depth-resolved numerical model that can describe the vertical profiles of the dynamic characteristics is developed based on the Herschel-Bulkley rheology to study the unsteady mud flows with a free surface. The proposed numerical

model is validated with experiments carried out in this study, the steady-state solution for uniform flows, and cases simulated by other numerical models. On the basis, the interactions between the mud flows and structures are studied and analyzed.

## 2 Mathematical Formulation

### 2.1 Governing equations

Mud flows are usually considered to be incompressible fluids (Li et al. 2018; Jing et al. 2018). Thus, the governing equations of mud flows are formulated as

$$\nabla \cdot \bar{u} = 0 \tag{1}$$

$$\frac{\partial \bar{u}}{\partial t} + \bar{u} \cdot \nabla \bar{u} = -\nabla p + \frac{1}{\rho}\nabla \cdot \boldsymbol{\tau} + \bar{g} \tag{2}$$

where $\bar{u}$, $p$ and $\boldsymbol{\tau}$ are the bulk velocity field, pressure field and shear stress tensor, respectively. $\rho$ denotes the density of the mud fluid, $\bar{g}$ represents the acceleration due to gravity; $\nabla\cdot$ and $\nabla$ are the divergence and gradient operators, respectively.

### 2.2 Closure to stress tensor

For Herschel-Bulkley fluids, the rheological characteristics of shear-thinning are considered and the rheology in the laminar regime is determined as follows:

$$\boldsymbol{\tau} = \tau_y \frac{\mathbf{D}}{\|\mathbf{D}\|} + 2^n \eta_n \|\mathbf{D}\|^{n-1}\mathbf{D} \tag{3}$$

where $\boldsymbol{\tau}$ is the Cauchy stress tensor; $\mathbf{D} = (\nabla\bar{u} + (\nabla\bar{u})^T)/2$ is the strain rate tensor; $\|\mathbf{D}\| = \sqrt{[tr(\mathbf{D}^2) - (tr\mathbf{D})^2]/2}$ represents the square root of the second invariant of the strain rate tensor, where $tr\mathbf{D} = \nabla \cdot \bar{u} = 0$, and $tr$ is the trace of the tensor; $\tau_y$ is the yield stress; $\eta_n$ is the consistency of fluid with dimension [ $ML^{-1}T^{n-2}$ ]; $n$ is the flowing index, a measure of the shear-thinning magnitude that varies from zero to unity, where the upper limit of $n = 1$ corresponds to a Bingham fluid; and $\eta_1$ represents the regular dynamic viscosity. The stress tensor of a Bingham fluid can thus be formulated as

$$\boldsymbol{\tau} = \tau_y \frac{\mathbf{D}}{\|\mathbf{D}\|} + 2\eta_1 \mathbf{D} \tag{4}$$

Furthermore, the apparent viscosity $\mu_e$ of a Herschel-Bulkley fluid can be defined as

$$\mu_e = \frac{\tau_y}{\|\mathbf{D}\|} + 2^n \mu \|\mathbf{D}\|^{n-1} \tag{5}$$

Although no general critical criterion exists for the transition from the laminar regime to the turbulent regime, some attempts have been made to propose various criteria, such as turbulent models for Herschel-Bulkley fluids and Bingham fluids. A popular empirical criterion was proposed by Qian and Wan (1986) as follows:

$$\frac{1}{Re_B} = \frac{1}{Re_\tau} + \frac{1}{Re_\mu} < 2100 \tag{6}$$

where $Re_\tau = 8\rho U^2/\tau_y$ represents the ratio of the inertial stress to the yield stress, $Re_\mu = 4\rho UH/\mu$ represents the ratio of the inertial stress to the viscous stress, and $U$ and $H$ are the characteristic velocity and characteristic depth, respectively.

However, several field studies have shown that the Reynolds number of mud flows is reasonably small and that mud flows can be identified as laminar flows with the rheological behaviour of either Herschel-Bulkley or Bingham fluids (Wang et al. 2014; Li et al. 2018).

## 3 Numerical Methods

The two-step projection method, which has been widely used in the literature (Chorin 1967; Lin et al. 1998; Lagrée et al. 2011), was implemented to solve the numerical model (Eqs. (1)-(3)) with the finite difference method. The mesh system was staggered, and the vectors were defined at the edge of the grid, while the scalars were defined at the centre of the grid. An intermediate velocity $\bar{u}^*$ was introduced during the two-step projection method to carry the correct vorticity:

$$\frac{\bar{u}^* - \bar{u}^N}{\Delta t} = -\bar{u}^N \cdot \nabla\bar{u}^N + \nabla \cdot [\alpha\mu_e^N \mathbf{D}^N + (1-\alpha)\mu_e^N \mathbf{D}^*] + \bar{g} \tag{7}$$

where $\Delta t$ is the time step size, $N$ is the current time step and $\alpha$ is a weight coefficient for the Crank-Nicson (C-N) scheme that is used to discretize the stress term. The C-N scheme becomes explicit when $\alpha = 1$ and

implicit when $\alpha = 0$.

Then, to avoid the singularity of the apparent viscosity $\mu_e$ of Herschel-Bulkley fluids in Eq. (5), the simple regularization procedure proposed by Frigaard and Nouar (2005) is employed:

$$\mu_e^N = \frac{\tau_y}{\|\mathbf{D}_N\| + \varepsilon} + 2^n \frac{\mu}{(\|\mathbf{D}_N\| + \varepsilon)^{1-n}} \quad (8)$$

where $\varepsilon$ is taken as $10^{-6}$ s$^{-1}$ in the present study.

Generally, two stability criteria for the time step size are necessary to solve Eq. (7) with numerical stability. One criterion is associated with the convective term, which can be characterized as the Courant number $C_r$:

$$\Delta t \leq \min\{\frac{Cr \times \Delta x}{u_{\max}}, \frac{Cr \times \Delta y}{v_{\max}}\} \quad (9)$$

For the C-N scheme with $\alpha \geq 1/2$, the time step size must satisfy the following criterion,

$$\Delta t \leq \min\{\frac{\rho \Delta x^2}{6\mu_e}, \frac{\rho \Delta y^2}{6\mu_e}\} \quad (10)$$

Thus, a very small time step is needed due to the significantly large effective viscosity of mud flows. However, a smaller time step is accompanied by an increased computational cost. Therefore, the value of $\alpha$ was chosen to be $\alpha = 0$ to reduce the computation time in the proposed model. Accordingly, Eq. (7) can be changed to be

$$\frac{\vec{u}^* - \vec{u}^N}{\Delta t} = -\vec{u}^N \cdot \nabla \vec{u}^N + \nabla \cdot (\mu_e^N \mathbf{D}^*) + \vec{g} \quad (11)$$

To decouple the scalar equations for each velocity component, the second term on the right side of Eq. (11) can be approximately expanded as

$$\nabla \cdot (\mu_e^N \mathbf{D}^*) \approx \frac{1}{2}\nabla \cdot [\mu_e^N (\nabla \vec{u}^* + (\nabla \vec{u}^N)^T)] \quad (12)$$

Based on the general tensorial identity, the following equality is valid:

$$\begin{aligned}
&\frac{1}{2}\nabla \cdot (\mu_e^N (\nabla \vec{u}^N)^T) \\
&= \frac{1}{2}\nabla \mu_e^N \cdot (\nabla \vec{u}^N)^T + \frac{1}{2}\mu_e^N \nabla \cdot (\nabla \vec{u}^N)^T \\
&= \frac{1}{2}\nabla \mu_e^N \cdot (\nabla \vec{u}^N)^T + \frac{1}{2}\mu_e^N \nabla (\nabla \cdot \vec{u}^N) \\
&= \frac{1}{2}\nabla \mu_e^N \cdot (\nabla \vec{u}^N)^T
\end{aligned} \quad (13)$$

where the incompressibility condition $\nabla \cdot \vec{u}^N = 0$ is used in Eq. (13). When the yield stress vanishes, the effective viscosity is a constant and its gradient is zero.

Substituting Eqs. (12) and (13) into Eq. (11), the final intermediate velocity can be solved as follows:

$$\begin{aligned}
&\frac{\vec{u}^* - \vec{u}^N}{\Delta t} - \frac{1}{2}\nabla \cdot (\mu_e^N \nabla \vec{u}^*) \\
&= -\vec{u}^N \cdot \nabla \vec{u}^N + \frac{1}{2}\nabla \mu_e^N \cdot (\nabla \vec{u}^N)^T + \vec{g}
\end{aligned} \quad (14)$$

where the second term on the left-hand side of Eq. (14) can be discretized by the second-order central difference scheme. In addition, the first term on the right-hand side, namely, the velocity advection term, can be discretized by combining the upwind scheme with the central difference scheme (Lin et al. 1998). For each velocity component, the scalar components in Eq. (14) were solved separately with the biconjugate gradient stabilized (Bi-CGSTAB) method, which is a robust method for solving linear algebraic equations (Van der Vorst 1992).

Then, the intermediate velocity field $\vec{u}^*$ is projected onto the divergence-free space to obtain the final velocity $\vec{u}^{N+1}$, which satisfies the continuity equation, i.e., $\nabla \cdot \vec{u}^{N+1} = 0$. Thus, the second step of the projection method is

$$\frac{\vec{u}^{N+1} - \vec{u}^*}{\Delta t} = -\frac{1}{\rho^{N+1}}\nabla p^{N+1} \quad (15)$$

$$\nabla \cdot \vec{u}^{N+1} = 0 \quad (16)$$

Combining Eq. (14) with Eq. (15) indicates that the velocity field $\vec{u}^{N+1}$ simultaneously satisfies the momentum equation and the continuity equation.

According to Eq. (16), the divergence operator can be applied to Eq. (15), and the pressure Poisson equation can be obtained as follows:

$$\nabla \cdot (\frac{1}{\rho^{N+1}}\nabla p^{N+1}) = \frac{1}{\Delta t}\nabla \cdot \vec{u}^* = 0 \quad (17)$$

When the intermediate velocity $\vec{u}^*$ is solved, Eq. (17) can be discretized as a set of linear algebraic equations based on the central difference method. Then, the pressure at the $N+1$-th time step can be obtained iteratively with the Bi-CGSTAB method (Van der Vorst 1992). Then, the final correct velocity at the $N+1$-th time step can be solved by Eq. (15) with the obtained pressure.

The free surface of the mud flows considered in the present study was tracked by the volume of fluid (VOF) method (Hirt and Nichols 1981), which is expressed as

$$\frac{\partial F}{\partial t} + \vec{u} \cdot \nabla F = 0 \qquad (18)$$

where $F$ represents the ratio of the volume occupied by the mud flow to the entire volume of the grid cell. The value of $F$ ranges from 0 to 1; when $F$ is equal to 1, the entire cell is filled by the mud flow and when $F$ is equal to 0, the cell is empty.

## 4 Laboratory Experiments

### 4.1 Experimental setup

To validate the numerical model for simulating mud flows with the Herschel-Bulkley rheology, a series of laboratory experiments involving dam break mud flows were conducted on the Wangjiang Campus, Sichuan University. The flume was 3.0 m long, 0.23 m wide and 0.25 m high (Fig. 1), and the mud material container was 0.48 m long, 0.23 m wide and 0.40 m high. The lateral sides and bottom of the flume were made of smooth and transparent acrylic plates to avoid the formation of broken fluids and to easily observe the motion of mud flows. As shown in Fig. 1, two XY-14SY pressure sensors were installed at the bottom of the flume bed at positions of $x = 1.5$ m (upstream section) and $x = 2.5$ m (downstream section) to record the bottom pressure. The sampling frequency and the accuracy of the pressure sensors were 50 Hz and 1 Pa/kPa, respectively. In addition, two ST-VL53L0X laser sensors were arranged at the same positions as the pressure sensors to capture the height of each mud flow because the mud is not transparent. The sampling frequency and the accuracy of the laser sensors were 20 Hz and 1 mm/1 m, respectively.

The particle matrices for the mud slurry used in the laboratory experiments were collected from Duiwoliang gully, which is a mud flow gully located in Pingwu County, Mianyang city, Sichuan Province, on the right bank upstream of the Fujiang River. The maximum particle size of the mud slurry was 2 mm after sieving, and the full particle size distribution of the mud slurry with a median particle size of 0.1 mm is shown in Fig. 2. The rheology of the slurry samples with a density of $\rho = 1600$ kg/m³ was measured by an Anton Paar rotational rheometer. The rheological measurements are plotted in Fig. 3 as red circles. Then, the measured points were fitted with the Herschel-Bulkley model. The fitting line

approximately passed through all the measured points, suggesting that the yield stress $\tau_y$, flow index $n$ and consistency coefficient $\eta_n$ of the fluid for the collected mud slurry were 5.01 Pa, 0.37 and 2.04 Pa·s^0.37, respectively.
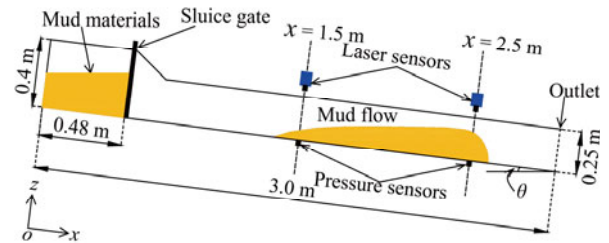
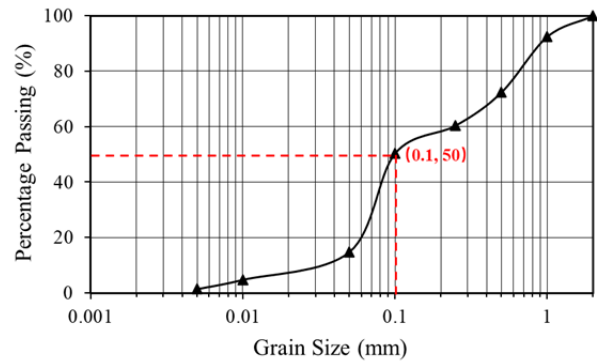

**Fig. 1** Schematic drawing of the experimental flume.


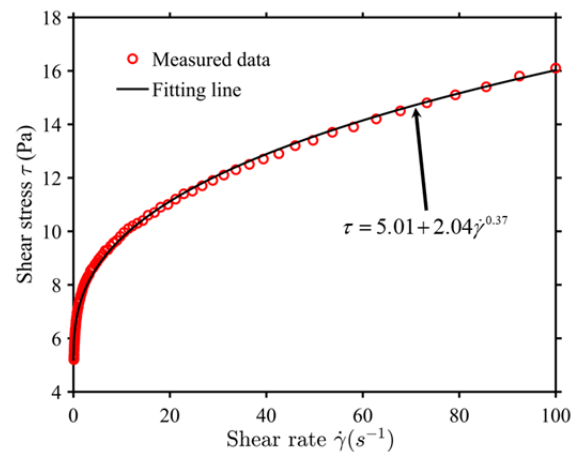
**Fig. 2** Grading of particles in the mud materials



**Fig. 3** Rheological measurements of the mud samples used in the flume experiment fitted by the Herschel-Bulkley model.

The slope of a laboratory flume typically ranges from 0° to 15° (Cui et al. 2005; Chen et al. 2018). Thus, the flume slope ($\theta$) was set to be 0°, 5° and 10° to simulate different cases during the experiments, as illustrated in Fig. 1. The mud materials with a density of $\rho = 1600$ kg/m³ were initially prepared and placed in
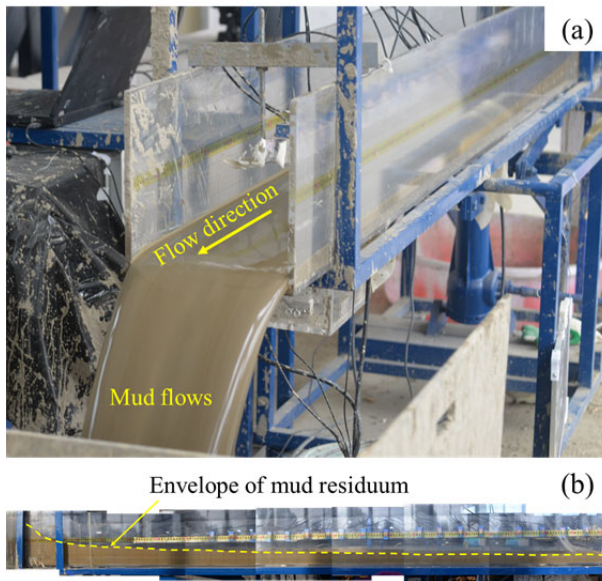
**Fig. 4** Test procedure: (a) mud material flows along the flume; (b) envelope of the mud residuum.

the container. The volumes of mud materials with flume slopes of 0°, 5° and 10° were 0.0386 m³, 0.0363 m³ and 0.0340 m³, respectively, when the length of the mud material container was set to be 0.48 m.

## 4.2 Results

During the experiments, the sluice gate was opened, and the mud materials behind the sluice gate flowed along the flume (Fig. 4(a)). The envelope of the mud residuum on both lateral sides of the channel is usually determined as the maximum height of mud flows in the field (Cui et al. 2005). Likewise, the mud

residuum was chosen as the maximum height on the lateral sides of the flume in the laboratory experiments. The envelopes of mud residuum for all the experiments were measured by a steel ruler after the mud flows ceased (Fig. 4(b)).

For slopes inclined at 0°, 5° and 10°, the pressure time histories at the bottom of the flume and the heights of the mud flows recorded by the two pressure sensors and two laser sensors at the positions $x$ =1.5 m and 2.5 m are separately shown as red circles in Fig. 5, Fig. 6 and Fig. 7. The experimental data of the envelopes of the mud residuum are shown in Fig. 8 for cases with three different slopes.

Based on the experimental data, the maximum heights $H_{max}$ and maximum bottom pressures $P_{bmax}$ measured at the positions $x = 1.5$ m and $x = 2.5$ m are summarized in Table 1. The results reveal that as the driving stress increased (i.e., the stress acting on the mud flows) due to a larger angle of inclination, the smaller the values for both $H_{max}$ and $P_{bmax}$ (Fig. 9(a)). In addition, the time at which the mud flows front arrived at $x = 1.5$ m, denoted $T_{1.5}$, decreased, and $U_m$, which represents the mean velocity of the front propagating from $x = 1.5$ m to $x = 2.5$ $m$ increased when the flume slope increased from 0° to 10° due to the corresponding increase in the driving stress (Fig. 9(b)). Unlike pure water flows, mud flows can stop on an inclined slope when the driving stress is less than the resistance. When the slope was inclined more than 0°, the stop heights $H_{stop}$ of the mud flows on the flume bed were constant along the flow direction and decreased as the inclination increased. However, for the 0° slope cases, $H_{stop}$ was not constant and decreased along the flow direction (Fig. 9(c)).
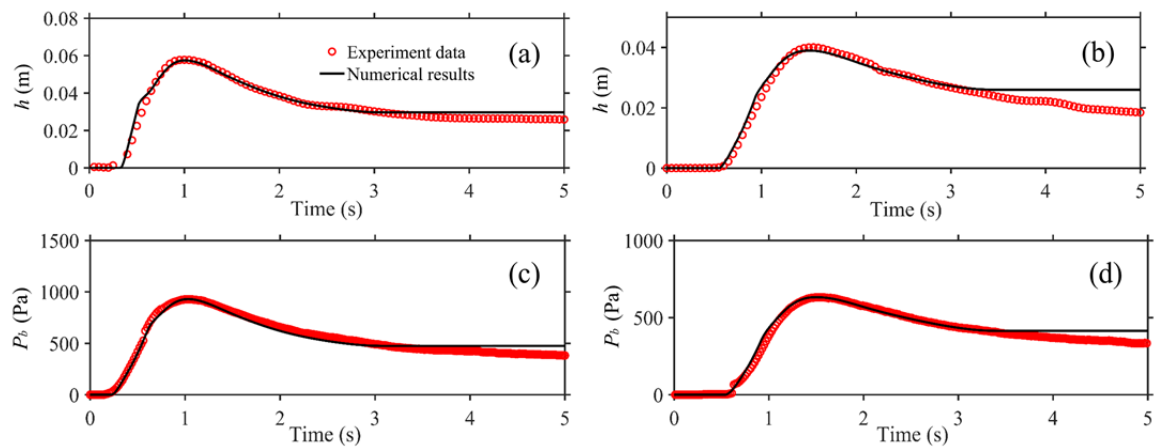


**Fig. 5** Comparisons of the time histories of the mud flow height and bottom pressure between the numerical results (black solid line) and the flume experiment results (red circles) when the slope of the flume was inclined at 0°: (a) height at $x = 1.5$ m, (b) height at $x = 2.5$ m, (c) pressure at $x = 1.5$ m, and (d) pressure at $x = 2.5$ m.
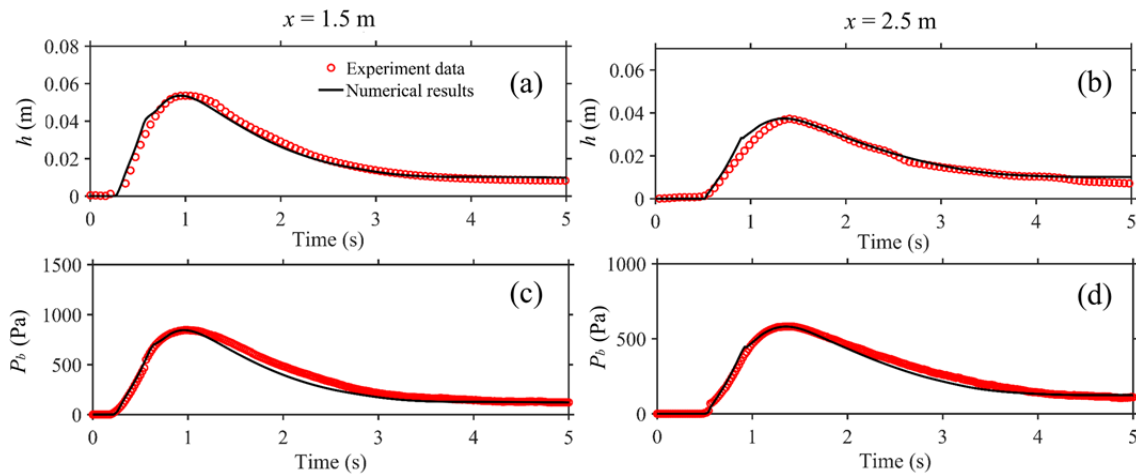
**Fig. 6** Comparisons of the time histories of the mud flow height and bottom pressure between the numerical results (black solid line) and the flume experiment results (red circles) when the slope of the flume was inclined at 5°: (a) height at $x$ = 1.5 m, (b) height at $x$ = 2.5 m, (c) pressure at $x$ = 1.5 m, and (d) pressure at $x$ = 2.5 m.
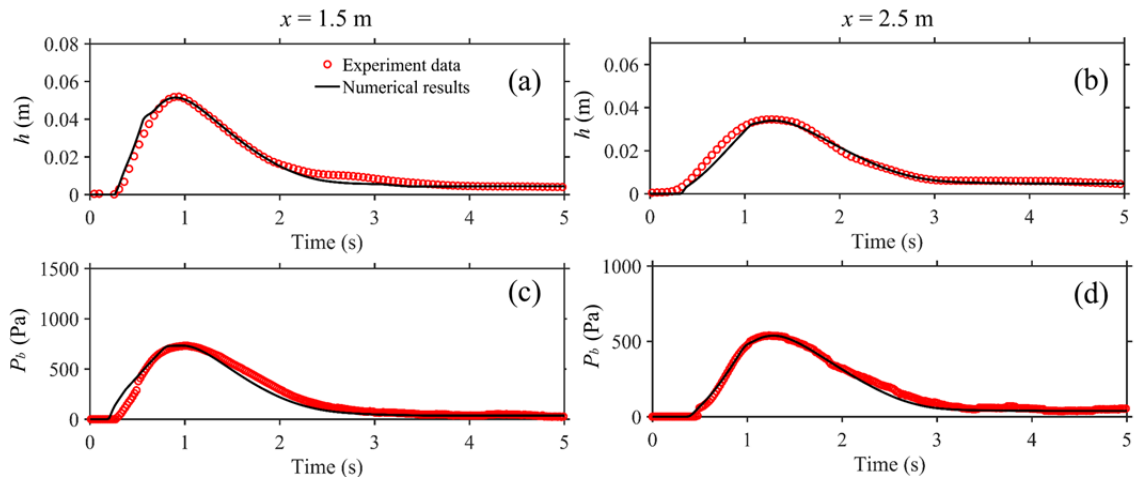


**Fig. 7** Comparisons of the time histories of the mud flow height and bottom pressure between the numerical results (black solid line) and the flume experiment results (red circles) when the slope of the flume was inclined at 10°: (a) height at $x$ = 1.5 m, (b) height at $x$ = 2.5 m, (c) pressure at $x$ = 1.5 m, and (d) pressure at $x$ = 2.5 m.

**Table 1** Dynamic parameters of the mud flows measured during the experiments on slopes inclined at 0°, 5° and 10°

| Slope(°) | $H_{max}$ (1.5) (m) | $H_{max}$ (2.5)(m) | $P_{bmax}$ (1.5) (m) | $P_{bmax}$ (2.5)(m) | $T_{1.5}$(s) | $U_m$ (m/s) | $H_{stop}$(m) |
|---|---|---|---|---|---|---|---|
| 0 | 0.058 | 0.040 | 928.0 | 631.8 | 0.25 | 2.85 | $H_{stop}$(1.5) = 0.026; $H_{stop}$(2.5) = 0.019 |
| 5 | 0.054 | 0.037 | 844.6 | 581.5 | 0.22 | 3.04 | 0.007 |
| 10 | 0.052 | 0.033 | 731.7 | 538.1 | 0.20 | 3.63 | 0.005 |

**Note:** $H_{max}(x)$, $P_{bmax}(x)$ and $H_{stop}(x)$ are the maximum height, maximum bottom pressure and stop height, respectively, at position $x$, where $x$ = 1.5 m and 2.5 m; $T_{1.5}$ is the time at which the mud flow arrives at $x$ = 1.5 m; and $U_m$ is the mean front velocity from $x$ = 1.5 m to $x$ = 2.5 m.

## 5 Numerical Validations

### 5.1 Comparisons with the steady-state solution for uniform flows

The steady-state solution for uniform flows is usually used to validate the numerical model.

However, the flume slope for a steady and uniform mud flow with a free-surface should not be zero, as the gravity component is needed to balance the resistance of mud flows and to maintain the uniform conditions. As proposed by Huang et al. (1998), the theoretical velocity profiles of Herschel-Bulkley fluids under steady and uniform conditions assuming

hydrostatic pressure can be formulated as

$$u = \begin{cases} \dfrac{n}{n+1}(\dfrac{\rho g H^{n+1}\sin\theta}{\eta_n})^{1/n}[1-(1-\dfrac{z}{H})^{(n+1)/n}], & ,if \quad 0\le z\le H \\ \dfrac{n}{n+1}(\dfrac{\rho g H^{n+1}\sin\theta}{\eta_n})^{1/n}, & ,if \quad H\le z\le h \end{cases} \quad (19)$$

where $u$ is the velocity in the $x$-direction, $h$ is the flow height, $\rho$ is the density of the flow, $H$ is the thickness of the shear layer (Fig. 10), $\theta$ is the slope of the bed, and the physical meanings of $\eta_n$ and $n$ are the same as in Eq. (3).
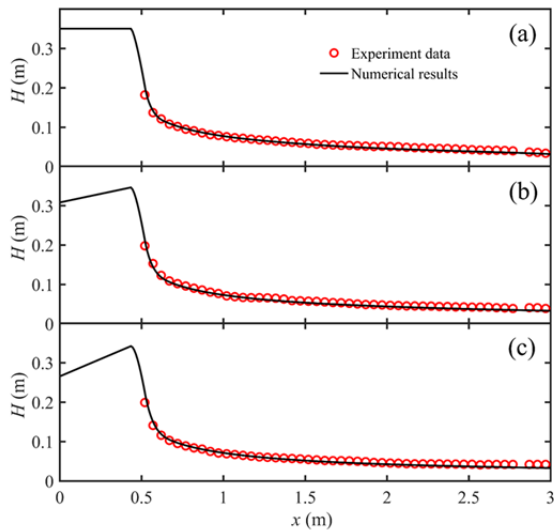


**Fig. 8** Comparison of the envelope of the mud residuum from the hopper to the outlet along the flume between the numerical results and experimental data at flume inclination angles of (a) 0°, (b) 5°, and (c) 10°.

The value of $n$ should not be zero; otherwise the shear layer for Herschel-Bulkley fluids would disappear, as sketched in Fig. 10. The thickness of plug layer $H_p$ can be determined as

$$H_p = h - H = \frac{\tau_y}{\rho g \sin\theta} \quad (20)$$

According to Eq. (20), $H_p$ depends only on the fluid density and yield stress when the inclination angle $\theta$ is fixed.

In this validation, a steady and uniform flow of Herschel-Bulkley fluids was considered with a flow height of $h$ =0.2 m, an inclination angle of 1°, a flowing index of $n$ = 0.5, a fluid density of 1000 kg/m³, and a yield stress of 100 Pa, a consistency of 1 Pa·s⁰·⁵. Thus, the plug layer thickness $H_p$ was calculated to be 0.117 m based on Eq. (20), and the shear layer thickness $H$ was 0.083 m. The computational domain was $x$=0.5 m by $z$=0.25 m with grid sizes of $\Delta x$ = 0.002 m and $\Delta z$ = 0.001 m. The time-step was fixed at
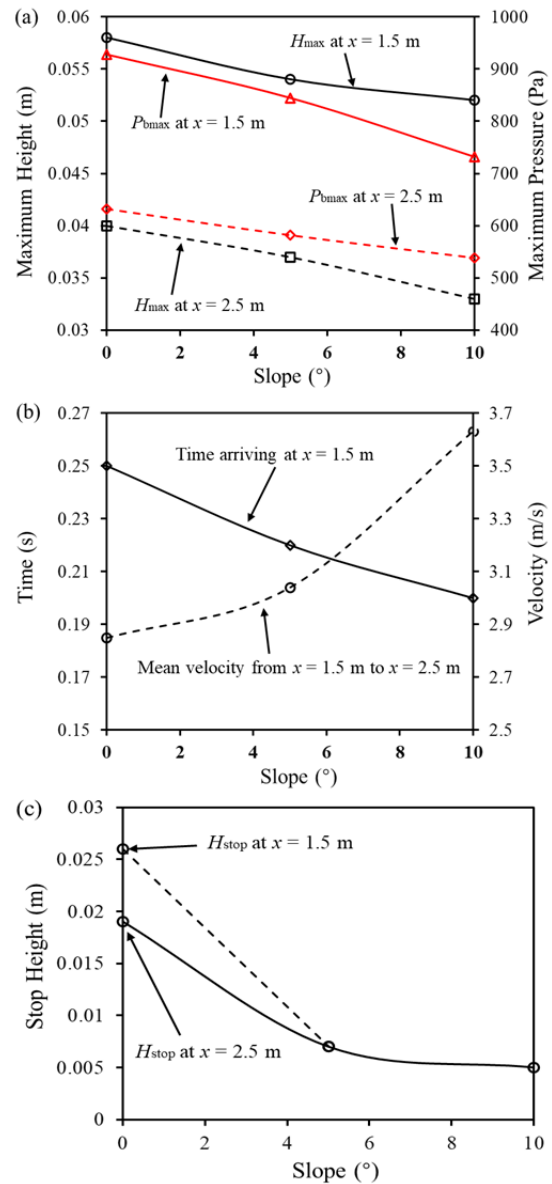


**Fig. 9** Tendencies of the dynamic parameters of the mud flows as the inclination angle increases.

0.0001 s to ensure numerical stability.

The results of the comparison between the simulated velocity profiles and the theoretical velocity profiles are shown in Fig. 11, illustrating that the present model can accurately simulate the velocity profiles for both the plug layer and the shear layer.

## 5.2 Comparisons with experiments of mud dam break flows

The initial dimensions and rheological parameters for the numerical model were set to be the same as those in the laboratory experiments (Fig. 1

and Fig. 3) for the numerical validation. Thus, the yield stress $\tau_y$, flow index $n$ and consistency coefficient $\eta_n$ of the dam break mud flows were 5.01 Pa, 0.37 and 2.04 Pa·s^0.37, respectively. The computational domain for the numerical cases was $x$ = 3 m by $z$=0.6 m and the grid sizes were taken as $\Delta x$ = 0.01 m and $\Delta z$ = 0.003 m. The time-step was fixed at $\Delta t$ = 0.001 s to ensure the numerical stability. The boundary conditions of the downstream outlet were set as the outflow boundary conditions, i.e., $\partial \bar{u} / \partial \bar{n} = 0$, where $\bar{n}$ denotes the unit outer normal vector at the downstream boundary. No-slip boundary conditions were implemented at the bottom.
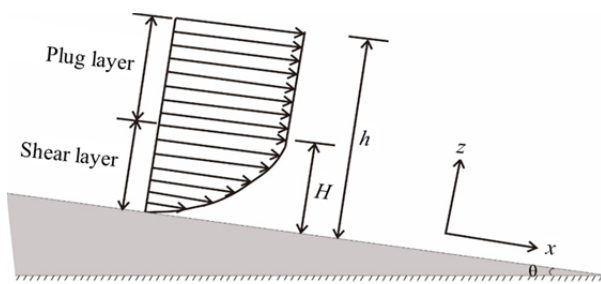


**Fig. 10** Schematic diagram of the velocity profile of a Herschel-Bulkley fluid under a steady and uniform flow regime.
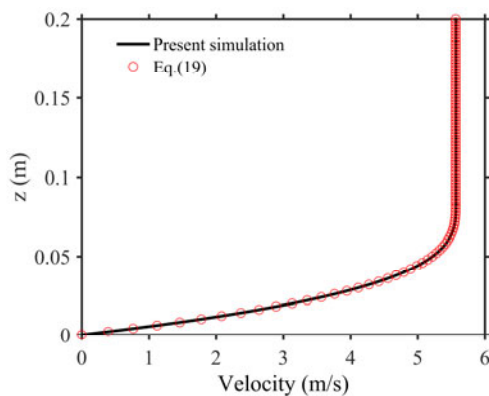


**Fig. 11** Comparison of the flow velocity profiles between the simulated results and the analytical solution under a steady and uniform flow regime.

The results of comparisons among the simulated time histories of the dam break mud flow height and bottom pressure at the upstream ($x$ =1.5 m) and downstream ($x$ = 2.5 m) positions with the corresponding measurements in the cases with slopes of 0°, 5° and 10° are shown in Fig. 5, Fig. 6 and Fig. 7, respectively.

Fig. 5 shows that the movement of the dam break mud flows lasted approximately 3.2 s in the laboratory experiments and the numerical results agree well with the experimental data during the first

3 s for the case with a 0° flume slope. After 3 s, however, the calculated time histories of the mud flows height and bottom pressure significantly deviate from the measured data, while the simulated results remain constant, and the experimental data show a decreasing tendency. The reason is that the dam break mud flows stopped after 3 s in the numerical model, whereas they did not fully stop in the laboratory experiments. The mud materials used in the laboratory experiments consisted of particles with different grain sizes and water. Thus, the water in mud flows permeated out of the slurry after the dam break mud flow stopped due to the settlement of particles, which would result in gradual reductions in both the height and the bottom pressure. Nevertheless, for the cases with 5° and 10°, the simulated heights and bottom pressures agree well with the measured results, even after 3 s, as shown in Fig. 6 and Fig. 7.

Likewise, the simulated envelopes of the mud residuum were compared with the experimental measurements for the three cases with different flume slopes ($\theta$= 0°, 5° and 10°), as shown in Fig. 8. The simulated results show good agreement with the experimental data starting from $x$ = 0.5 m, where the numerical model suggests that a maximum mud residuum height is observed at nearly $x$ = 0.48 m.

Overall, the simulated results of the numerical model developed herein were consistent with the laboratory measurements for dam break flows consisting of a Herschel-Bulkley slurry, verifying that this numerical model is applicable for simulating Herschel-Bulkley fluids.

### 5.3 Comparisons with other numerical results

Li et al. (2018) simulated dam break flows on a horizontal plane with Herschel-Bulkley rheology through OpenFOAM. The initial height of the dam break flows was $H$=0.6 m, and the initial length was $L$=0.9 m, as sketched in Fig. 12. In their numerical simulation, the density of the fluid was 1000 kg/m³, and for the Hershel-Bulkley rheology, the yield stress, consistency and flow index were 30.0 Pa, 4.279 Pa·s^0.479 and 0.479, respectively. The model developed in the present study was further validated with the case simulated by Li et al. (2018). The computational domain for the proposed model was $x$ = 4 m by $z$ = 0.8 m with the grid sizes of $\Delta x$ = 0.01 m and $\Delta z$ = 0.004 m. The time-step was fixed at 0.001 s to ensure
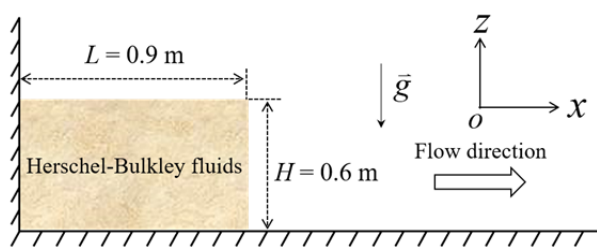
**Fig. 12** Initial configuration of the dam break of a Herschel-Bulkley fluid on a horizontal plane.
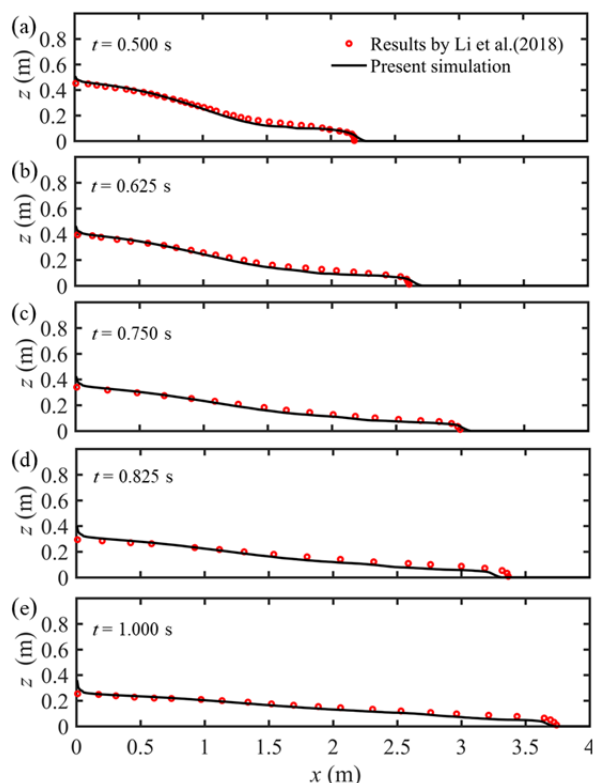


**Fig. 13** Comparisons of the instantaneous free surface profiles from the proposed numerical model (solid black line) and from Li et al. (2018) (red circles): at (a) $t$ = 0.500 s, (b) $t$ = 0.625 s, (c) $t$ = 0.750 s, (d) $t$ = 0.825 s, and (e) $t$ =1.000 s.

numerical stability.

Fig. 13 shows a comparison of the snapshots of the free surface profiles obtained by the proposed numerical model and by Li et al.'s (2018) model at 5 different times ($t$=0.500 s, 0.625 s, 0.750 s, 0.825 s and 1.000 s). In the proposed model, the no-slip boundary condition is employed, and then the fluid can adhere to the wall due to its high apparent viscosity of fluid. Overall, good agreement is observed for all 5 different times at every position, which suggests that the present model could well capture the strong variation in the free surface for Herschel-Bulkley fluids. However, Li et al. (2018) did not

analyze the vertical profiles of velocity and pressure due to a lack of measured profiles to validate them. Fortunately, the pressure, envelope of the mud residuum, velocity and variations in the free surface of the proposed model have been fully validated. Therefore, the proposed model is considered to be powerful tool for analysing the vertical profiles of velocity and pressure.

## 6 Dynamic Characteristics of Mud Flows in the Vertical Direction

### 6.1 Vertical velocity profiles of mud flows

The vertical profiles of velocity are crucial for understanding the dynamic properties of mud flows. However, the vertical profiles cannot be obtained in the traditional depth-averaged models because they remove the vertical information. The proposed model is a depth-resolved model and can obtain unsteady-state vertical profiles with nonuniform flows. In this study, the case of Li et al. (2018) is reproduced to illustrate the vertical profiles of mud flows. The computation domain, grid sizes, fixed time step and all fluid characteristics are the same as those in Li et al. (2018). The distributions of the pressure and velocity fields of dam break mud flows simulated by the proposed model are plotted at different instants in Fig. 14.

However, the vertical velocity profiles of real mud flows are highly sophisticated and are associated with an unsteady and nonuniform flow regime, for which it is almost impossible to obtain analytical solutions due to the strong nonlinearity of such flows. Numerical methods are good alternatives for determining the velocity profiles of mud flows while idealizing the properties of dam break flows to generate the unsteady and nonuniform flow regime of mud flows. To this end, in this study, dam break mud flows are numerically simulated. The vertical longitudinal velocity profiles at six different $x$ locations at $t$ = 1.5 s are plotted as solid lines in Fig. 15. The longitudinal velocity increases with an increase in the distance that the dam break flows have travelled. In addition, the plug layer of the mud dam break flows is present at $x$ = 3.0 m, where the shear layer is absent.

It is worth noting that the formation mechanism of the plug layer on the horizontal plane is different from that on an inclined slope. The longitudinal component of gravity serves to balance the fluid
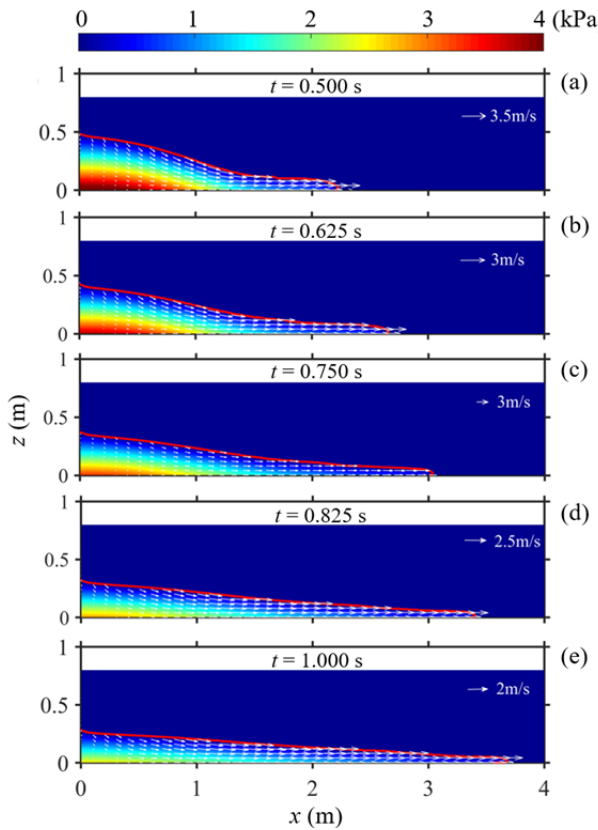
**Fig. 14** Snapshots of the distributions of the pressure and velocity fields of a dam breaking Herschel-Bulkley fluid on a horizontal plane at different moments, where the red line is the free surface, the white arrows indicate the velocity field, and the legend represents the pressure magnitude.

resistance on an inclined slope when steady and uniform flow conditions were maintained (Huang et al. 1998; Mei et al. 2001). In contrast, when the inclination angle is 0°, the steady and uniform flow condition cannot be satisfied in an open channel. As shown in Eq. (19), the velocity tends towards zero when the inclination angle $\theta$ equals 0°. On a horizontal surface, the longitudinal component of gravity vanishes, and the longitudinal component of the viscous stress can be balanced only by the longitudinal pressure gradient. However, a longitudinal pressure gradient is absent under steady and uniform flow conditions. Thus, the dam breaking mud flows gradually slow down and ultimately cease due to the presence of the longitudinal component of viscous stress.

Furthermore, based on the numerical results of the proposed model, the bottom shear stresses, flow depth and depth-averaged velocity at the position $x = 0.5$ m, $x = 1.0$ m, $x = 1.5$ m, $x = 2.0$ m, $x = 2.5$ m, $x = 3.0$ m with $t = 1.5$ s are listed in Table 2.

**Table 2** Values of the bottom shear stresses, flow depth, depth-averaged velocity, $U_p$ and $H$ under the steady uniform flow at different positions with $t = 1.5$ s

| Position $x$ (m) | $\tau_b$ (Pa) | $H$ (m) | $\bar{U}$ (m/s) | $U_p$ (m/s) | $H$ (mm) |
|---|---|---|---|---|---|
| 0.5 | 97.9 | 0.164 | 0.240 | 0.241 | 2.318 |
| 1.0 | 119.0 | 0.154 | 0.534 | 0.537 | 2.935 |
| 1.5 | 134.0 | 0.140 | 0.798 | 0.802 | 3.171 |
| 2.0 | 145.2 | 0.130 | 1.026 | 1.032 | 3.295 |
| 2.5 | 153.3 | 0.124 | 1.173 | 1.181 | 3.270 |
| 3.0 | 158.7 | 0.120 | 1.207 | 1.215 | 3.076 |

For the uniform flow, the velocity profile can be obtained from the Eq. (19) and can be reformulated as

$$u = \begin{cases} U_p[1-(1-\dfrac{z}{H})^{(n+1)/n}], if \quad 0 \le z \le H \\ U_p, \qquad\qquad\quad , if \quad H \le z \le h \end{cases} \quad (21)$$

where $H$ is the height of the shear layer; $U_p$ is the surface velocity, which can be formulated as

$$U_p = \frac{n}{n+1}(\frac{\rho g H^{n+1} \sin\theta}{\eta_n})^{1/n} \quad (22)$$

In this case, the bottom shear stress of Herschel-Bulkley fluids can be described as

$$\tau_b = \tau_y + \eta_n(\frac{\partial u}{\partial z})^n |_{z=0} \quad (23)$$

Substituting Eq. (21) into Eq. (23), the bottom shear stress can be reformulated as

$$\tau_b = \tau_y + \eta_n[\frac{n+1}{n}\frac{U_p}{H}]^n \quad (24)$$

When the bottom shear stress with the uniform flow is the same as the one obtained by the present simulation, and the same rheological parameters are employed, the $U_p/H$ can be calculated as

$$\frac{U_p}{H} = \frac{n}{n+1}(\frac{\tau_b - \tau_y}{\eta_n})^{1/n} \quad (25)$$

Furthermore, the depth-averaged velocity $\bar{U}$ of uniform flow can be calculated as

$$\bar{U} = \frac{1}{h}\int_0^h udz = \frac{1}{h}\int_0^H udz + \frac{1}{h}\int_H^h udz$$
$$= U_p(1 - \frac{n}{2n+1}\frac{H}{h}) \quad (26)$$

By combing Eqs. (25) and (26), $U_p$ and $H$ under the conditions of steady uniform flow with the same simulated bottom shear stress, flow depth and depth-averaged velocity can be calculated and listed in Table 2, where the flowing index $n$ is 0.479.

Substituting $U_p$ and $H$ into the Eq. (21), the velocity profiles under the steady uniform flow can be
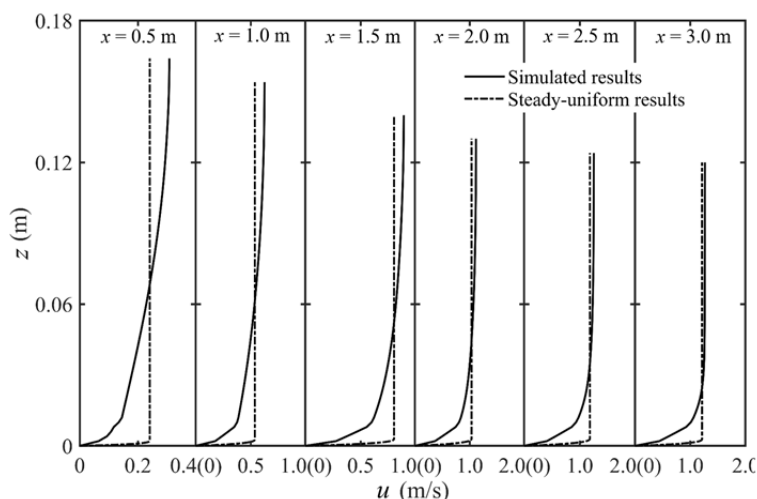
**Fig. 15** Profiles of the simulated longitudinal velocity of a dam break mud flow and the steady-state velocity with uniform flow at different positions with $t$ = 1.5 s.

plotted as dashed lines, as shown in Fig. 15. Comparing the simulated vertical profiles with the corresponding profiles obtained by employing steady uniform flow distribution under the conditions of the same actual bottom shear stress, flow depth and depth-averaged velocity show that the shear layers of steady uniform flows are less than those of simulated vertical profile. Furthermore, when the flows are fully developed, the velocity profiles of dam break mud flows are close to those of steady uniform flows.

**6.2 Impact pressure caused by mud flows**

The impact pressure, which is a crucial parameter for mitigating mud flows and developing appropriate countermeasures, is of great concern for studying the interaction between mud flows and obstacles (Tang et al. 2018). The dynamic responses of structures impacted by mud flows are usually associated with the impact pressure distribution (Cui et al. 2015; Liu et al. 2019). However, the impact pressures of mud flows are usually determined by the depth-averaged velocity because the detailed distribution of the impact pressure is quite difficult to be obtained (Liu et al. 2019). Armanini et al. (2011) argued that the impact pressures of mud flows are composed of hydrostatic pressure and dynamic pressure, where the former is related to the depth, while the latter depends on the velocity. Because the velocity distribution varies in both time and space, the dynamic pressure should also show spatiotemporal variations.

For convenience, a vertical structure with a height of 0.3 m and a thickness of 0.1 m located at $x$ = 2.5 m was added into Li et al.'s (2018) case to numerically study the interaction of mud dam break flows with a vertical structure on a horizontal plane. The computational domain, grid sizes, fixed time step and all fluid characteristics are the same as those described by Li et al. (2018).

As shown in Fig. 16, the distribution of the impact pressure on the upstream face of the structure varies with both time and height. The results show that the mud flows firstly impact the structure at $t$ = 0.56 s, and the maximum impact pressure emerges at $t$ = 0.58 s, when the height of mud flow is 0.72 m.

Furthermore, Fig. 16 demonstrates that the vertical position ($z$ = 0.075 m) of maximum impact pressure (15 kPa when $t$ = 0.58 s) is at neither the bottom nor the surface of the mud flows. Similar findings are observed in the experiments conducted by Cui et al. (2015).
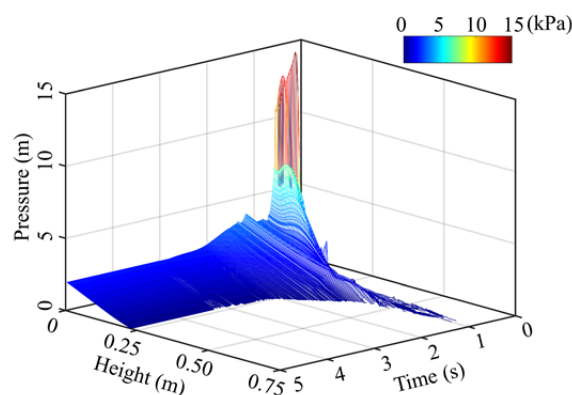


**Fig. 16** Impact pressure of dam break mud flows at $x$ = 2.45 m downstream from the container as a function of time and the height of the flow.

As shown in Fig. 17, the impact pressure firstly increases when the mud flows impact the structure (Fig. 17(a)). Then the mud flows raise along the surface of the structure and the free surface breaks (Fig. 17(b)), after which the raising mud flows collapse into the subsequent fluid and propagated downstream (as shown in Fig. 17(c)), and there is an instantaneous increase in the pressure of the mud flow at $t$=1.15 s (as shown in Fig. 16). Finally, as shown in Fig. 17(d), when the mud flows cease, the pressure on the
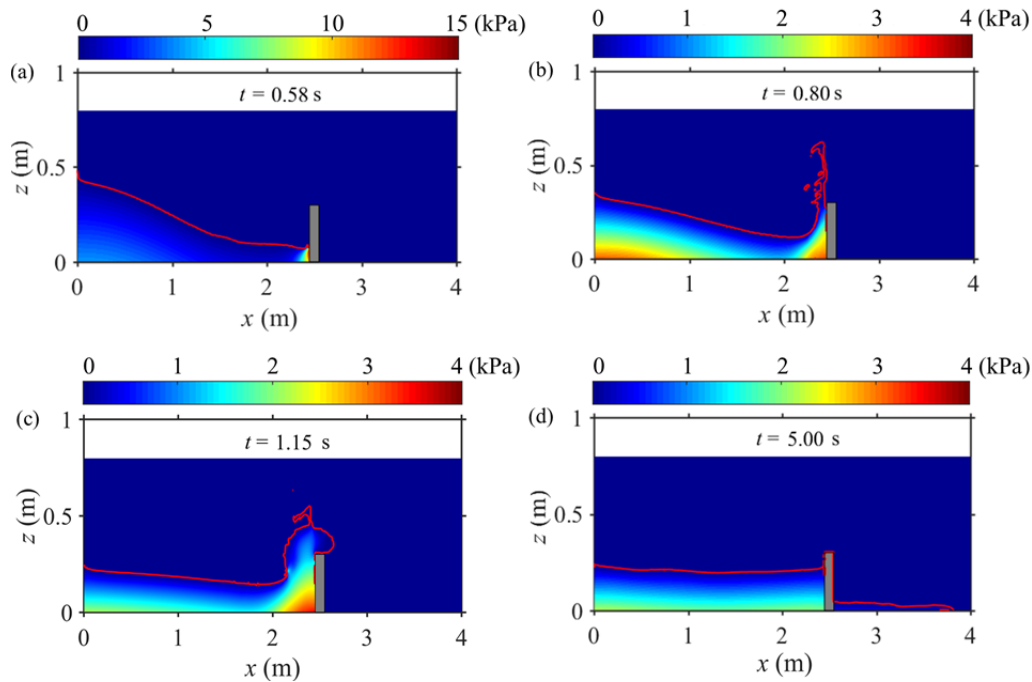
**Fig. 17** Distributions of the impact pressure of the Herschel-Bulkley fluid impacting the structure at different instants: (a) $t$ = 0.58 s, (b) $t$ = 0.80 s, (c) $t$ = 1.15 s, and (d) $t$ = 5.00 s (The red line is the free liquid level, and the legend represents the pressure magnitude).

structure became hydrostatic, and the magnitude of the pressure on the bottom of the flume was 2.23 kPa, where the height of the mud flow surface is 0.23 m.

Following Armanini et al. (2011), the total pressure $p$ of the mud flow can be decomposed into hydrostatic contribution $p_h$, which is calculated as $p_h = \rho g h$ (where $h$ is the height of mud flows) and dynamic contribution $p_d$. The dynamic pressure is obtained by subtracting the hydrostatic contribution



**Fig. 18** Profiles of the mud flow pressure and velocity with depth at $t$ = 0.58 s. The solid black line with squares represents the total pressure, the dotted line with circles represents the dynamic pressure, the dotted line represents the hydrostatic pressure, and the solid red line with squares represents the mud flow velocity.

from the total pressure ($p_d = p - p_h$). The vertical profiles of the velocity, total pressure and dynamic pressure and hydrostatic pressure at $t$ = 0.58 s are illustrated in Fig. 18. The velocity, total pressure and dynamic pressure firstly increase with increasing depth, and reach their peaks at $z$ = 0.075 m, then sharply decrease to zero when approaching to the free surface. The maximum total pressure, maximum dynamic pressure and maximum velocity are 15.00 kPa, 14.71 kPa and 3.66 m/s, respectively.

As suggested by Hu et al. (2011), the relationship between dynamic pressure $p_d$ and velocity can be described as,

$$p_d = K\rho u^2 \qquad (27)$$

in which $K$ is a dimensionless coefficient. In this case, $K$ was equal to 1.10 (not unity) according to the maximum dynamic pressure. The dimensionless coefficient may not be equal to unity if the mud flows that impact the structure are unsteady.

In addition, determining the location of the maximum dynamic pressure on a structure being impacted by a mud flow is extremely important, as this knowledge is indispensable for designing countermeasures and infrastructures (Liu et al. 2019). However, not all of the factors affecting the location of the maximum dynamic pressure are known. Thus, the effects of the yield stress and consistency coefficient,
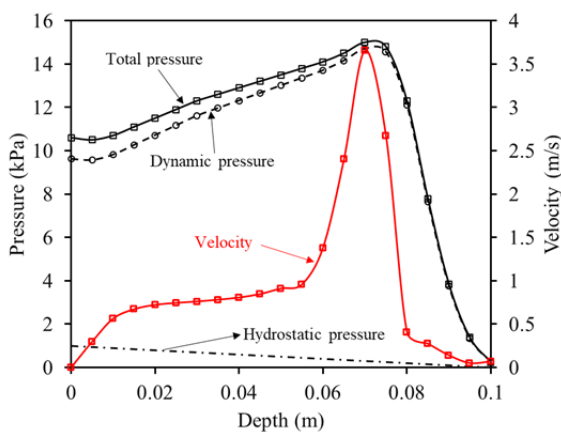
which are crucial parameters for the rheological characteristics of mud flows, on the location of maximum dynamic pressure are numerically studied. The rheological parameters used for the numerical tests and some simulated results (maximum dynamic pressure $P_{dmax}$, the normalized location $Z_{max}$, mud flow front velocity and dimensionless coefficient $K$) are listed in Table 3. The normalized location $Z_{max}$, which is illustrated in Fig. 19, can be calculated by the ratio of the location of the maximum dynamic pressure $z_{max}$ to the instantaneous surface height $h$:

$$Z_{max} = \frac{z_{max}}{h} \qquad (28)$$

**Table 3** Values of the rheological parameters used in the present simulations, the magnitude of the maximum dynamic pressure $P_{dmax}$, the normalized location $Z_{max}$ with the maximum dynamic pressure, the mud flow front velocity, and the dimensionless coefficient $K$ as formulated in Eq. (27)

| Case | Yield stress (Pa) | Consistency coefficient (Pa·s^{0.5}) | $P_{dmax}$ (kPa) | $Z_{max}$ | Front velocity (m/s) | $K$ |
|------|------|------|------|------|------|------|
| No.1 | 0.0 |  | 32.30 | 0.20 | 3.90 | 2.124 |
| No.2 | 1.0 |  | 17.90 | 0.30 | 3.80 | 1.239 |
| No.3 | 10.0 | 1.0 | 14.80 | 0.43 | 3.70 | 1.081 |
| No.4 | 50.0 |  | 10.90 | 0.47 | 3.21 | 1.064 |
| No.5 | 100.0 |  | 8.33 | 0.77 | 2.80 | 1.063 |
| No.6 |  | 0.1 | 19.50 | 0.40 | 3.80 | 1.350 |
| No.7 |  | 1.0 | 14.80 | 0.43 | 3.70 | 1.081 |
| No.8 | 10 | 10.0 | 13.19 | 0.47 | 3.49 | 1.077 |
| No.9 |  | 20.0 | 8.87 | 0.56 | 2.89 | 1.055 |
| No.10 |  | 30.0 | 7.07 | 0.83 | 2.59 | 1.046 |

The influences of the yield stress and consistency coefficient on the maximum dynamic pressure and front velocity are shown in Fig. 20(a) and Fig. 21(a), respectively. It can be easily seen that the maximum dynamic pressure and front velocity monotonically decrease with the increase of yield stress and consistency coefficient. This occurred because the effective viscosity rises with increases in the yield stress and consistency coefficient, which would lead to an increase in the dynamic resistance of the mudflow and consequently reduce both the front velocity and the maximum dynamic pressure. Additionally, the effects of the yield stress and consistency coefficient on the location of the maximum dynamic pressure and the dimensionless coefficient $K$ are shown in Fig. 20(b) and Fig. 21(b), respectively. The location of the maximum dynamic pressures increases but the dimensionless coefficient $K$ decreases with rises in the yield stress and consistency coefficient.
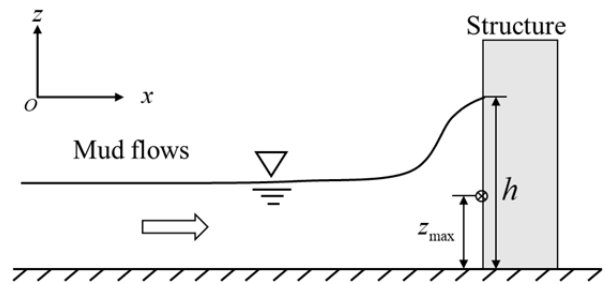


**Fig. 19** Sketch of mud flows impacting a structure, where $z_{max}$ denotes the location with the maximum dynamic pressure and $h$ is the instantaneous height of the mud flows.
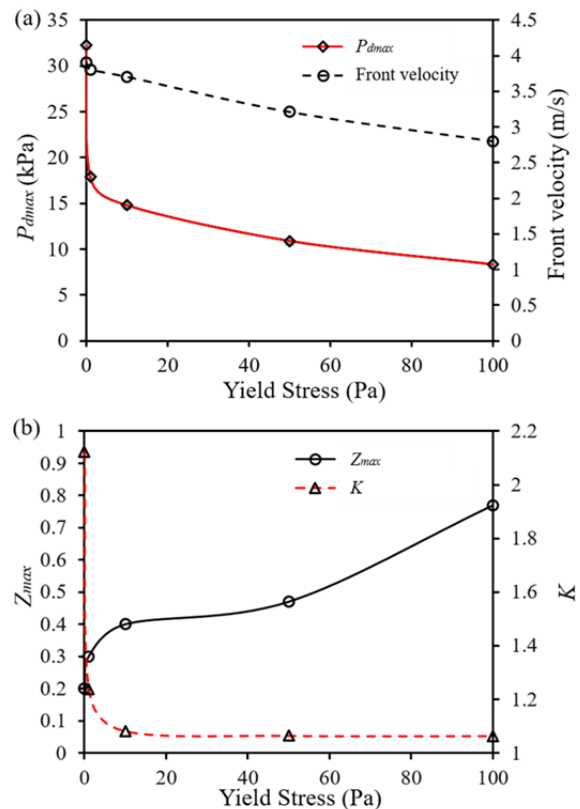


**Fig. 20** Change trends of the magnitude, normalized location of maximum dynamic pressure, front velocity of the mud flows and dimensionless coefficient $K$ with the yield stress.

Finally, the impact forces $F_{impact}$ exerted by the flow with the different rheological parameter listed in Table 3 on the entire wall can be calculated as

$$F_{impact} = \int_0^{H_w} p\,dz \qquad (29)$$

where $H_w$ is the height of the structure and is set as 0.3 m in this study. The time histories of the impact forces in the first 5 s for different consistencies and yield stresses of fluids are shown in Fig. 22. It can be seen from Fig. 22 that there are at least two peaks in
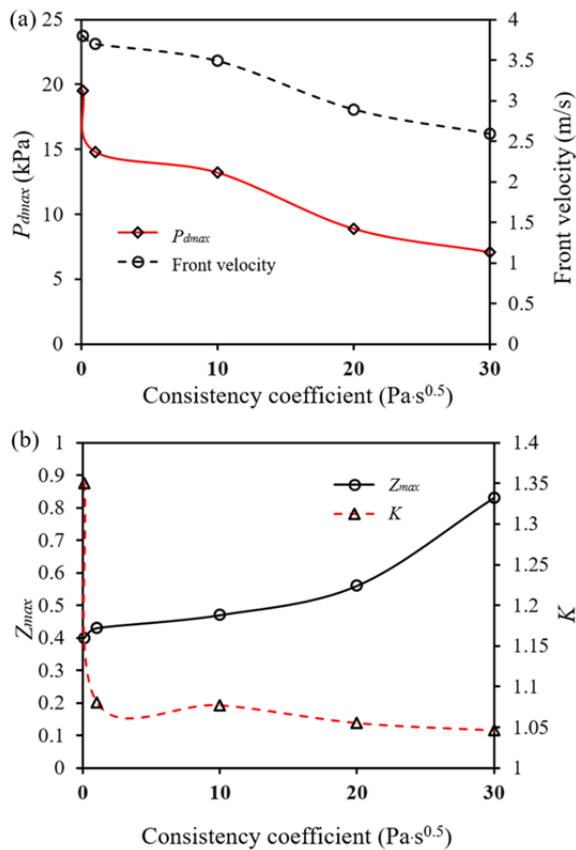
**Fig. 21** Change trends of the magnitude, normalized location of maximum dynamic pressure, front velocity of the mud flows and dimensionless coefficient $K$ with the consistency coefficient.

all of the simulated results. The first peak monotonically decreases with the increase of yield stress and consistency coefficient. The second peak is caused by an instantaneous high pressure when the raising fluid collapses into the subsequent fluid, which phenomenon is consistent with the previous discussion. The third peak occurs only at the low apparent viscosity, where the fluids can flow back and forth from the structure to left boundary of the computational domain. Furthermore, Fig. 22 shows that the fluids for the high apparent viscosity can rapidly cease after impacting the structure and at the final time the force exerting on the structure increases with the increase of apparent viscosity. This is caused by two reasons. Firstly, part of fluids can overtop the structure, which leads to a reduction in the volume of fluids exerting on the structure. And the lower the apparent viscosity, the more the volume of the overtopping fluids. Secondly, as the apparent viscosity increases, the mobility of the fluid decreases. For the high apparent viscosity, the surface of fluids is
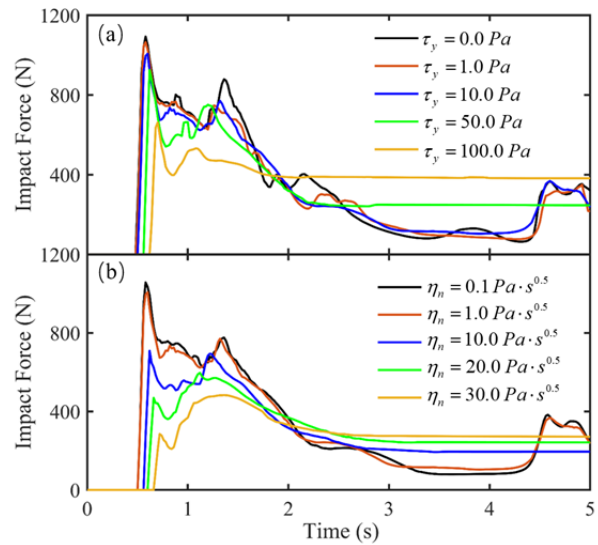


**Fig. 22** Time histories of impact forces in the first 5 s for different consistencies and yield stresses of fluids. (a) A consistency of 1 Pa·s$^{0.5}$ and different yield stresses; (b) A yield stress of 10 Pa and different consistencies.
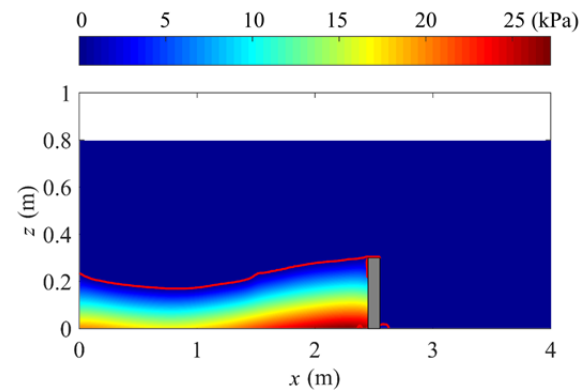


**Fig. 23** Inclined surface of fluids with respect to the horizontal plane when the fluids ceased upstream of the structure for a yield stress 100 Pa and a consistency 1 Pa·s$^{0.5}$.

inclined with respect to the horizontal plane when the fluids cease at the upstream of structure, as shown in Fig. 23. As the apparent viscosity increases, the inclination of the surface of fluids increases.

## 7 Conclusion

In this study, a 2D depth-resolved numerical model with Herschel-Bulkley rheology is developed to study unsteady and nonuniform mud flows by solving the Navier–Stokes equations. Additionally, a series of laboratory experiments involving dam break mud flows are conducted. The measured results show that

both the maximum heights and the maximum bottom pressures decrease with increasing inclination of the slope. The numerical model is fully validated in three ways: by the steady-state solution for uniform Herschel-Bulkley flows on an inclined plane, by the experimental results and by a comparison with other numerical results for dam break flows of Herschel-Bulkley fluids.

The vertical profiles of velocity and pressure are analysed and discussed with the validated numerical model. The simulated results show that the plug layer is formed for mud dam break flows, and the dynamic pressure dominates the whole pressure field. In addition, the location of the maximum impact pressure on the structure is at neither the bottom nor the surface of the mud flow. Moreover, further numerical tests show that the normalized location of

the maximum dynamic pressure will raise with increases of the yield stress and the consistency coefficient. The maximum dynamic pressure, the front velocity and dimensionless coefficient $K$ are also affected by those two rheological parameters and monotonically decrease as the values of those two parameters increase.

## Acknowledgements

## References

Ancey C (2006) Plasticity and geophysical flows: a review. J Non-Newton Fluid 142: 4-35.
https://doi.org/10.1016/j.jnnfm.2006.05.005

Ancey C, Iverson RM, Rentschler M, et al. (2008) An exact solution for ideal dam-break floods on steep slopes. Water Resour Res 44: W01430.
https://doi.org/10.1029/2007WR006353

Armanini A, Larcher M, Odorizzi M (2011) Dynamic impact of a debris flow front against a vertical wall. Proceedings of the 5th international conference on debris-flow hazards mitigation: mechanics, prediction and assessment, Padua, Italy: 1041-1049.
https://doi.org/10.4408/IJEGE.2011-03.B-113

Bartelt P, Buser O, Platzer K (2006) Fluctuation-dissipation relations for granular snow avalanches. J Glaciol 52(179): 631-643.
https://doi.org/10.3189/172756506781828476

Castro-Orgaz O, Hutter K, Giraldez JV, et al. (2015) Nonhydrostatic granular flow over 3‐D terrain: New Boussinesq‐type gravity waves?. J Geophys Res-Earth 120(1): 1-28.
https://doi.org/10.1002/2014JF003279

Chen C (1986) Generalized visco-plastic modeling of debris flow. J Hydraul Eng 114 (3): 237-258.
https://doi.org/10.1061/(ASCE)0733-9429(1988)114:3(237)

Chen HX, Zhang LM (2015) EDDA 1.0: integrated simulation of debris flow erosion, deposition and property changes. Geosci Model Dev 8(3): 829-844.
https://doi.org/10.5194/gmd-8-829-2015

Chen JG, Chen XQ, Zhao WY, et al. (2018) Debris flow drainage channel with energy dissipation structures: experimental study and engineering application. J Hydraul Eng 144(10): 06018012.
https://doi.org/10.1061/(ASCE)HY.1943-7900.0001523

Chorin AJ (1967) A numerical method for solving incompressible viscous flow problems. J Comput Phys 135(2):12-26.
https://doi.org/10.1006/jcph.1997.5716

Coussot, P (1997) Mudflow Rheology and Dynamics IAHR Monograph Series, Balkema.

Cui P, Chen X, Wang Y, et al. (2005) Jiangjia Ravine debris flows in south-western China. Debris-flow hazards and related phenomena. Springer Berlin Heidelberg: 565-594.
https://doi.org/10.1007/3-540-27129-5_22

Cui P, Zeng C, Lei Y (2015) Experimental analysis on the impact force of viscous debris flow. Earth Surf Proc Land 40(12): 1644-1655.
https://doi.org/10.1002/esp.3744

Cozzolino L, Pepe V, Morlando F, et al. (2017) Exact Solution of the Dam-Break Problem for Constrictions and Obstructions in Constant Width Rectangular Channels. J Hydraul Eng 143(11): 04017047.1-04017047.15.
https://doi.org/10.1061/(ASCE)HY.1943-7900.0001368

Delgado-Sánchez JM, Bouchut F, Fernández-Nieto ED, Mangeney A, Narbona-Reina G (2020) A two-layer shallow flow model with two axes of integration, well-balanced discretization and application to submarine avalanches. J Comput Phys 406: 109186.
https://doi.org/10.1016/j.jcp.2019.109186

Fan RL, Zhang LM, Wang HJ, et al. (2018) Evolution of debris flow activities in Gaojiagou Ravine during 2008–2016 after the Wenchuan earthquake. Eng Geol 235: 1-10.
https://doi.org/10.1016/j.enggeo.2018.01.017

Frigaard IA, Nouar C (2005) On the usage of viscosity regularisation methods for visco-plastic fluid flow computation. J Non-Newton Fluid 127(1): 1-26.
https://doi.org/10.1016/j.jnnfm.2005.01.003

Hirt CW, Nichols BD (1981) Volume of fluid (VOF) method for the dynamics of free boundaries. J Comput Phys 39: 201-225.
https://doi.org/10.1016/0021-9991(81)90145-5

Hu K, Wei F, Li Y (2011) Real–time measurement and preliminary analysis of debris‐flow impact force at Jiangjia Ravine, China. Earth Surf Proc Land 36(9): 1268-1278.
https://doi.org/10.1002/esp.2155

Huang X, García MH (1997) A perturbation solution for Bingham-plastic mudflows. J Hydraul Eng 123(11): 986-994.
https://doi.org/10.1061/(ASCE)0733-9429(1997)123:11(986)

Huang X, Garcia MH (1998) A Herschel–Bulkley model for mud flow down a slope. J Fluid Mech 374: 305-333.
https://doi.org/10.1017/S0022112098002845

Iverson RM (1997) The physics of debris flows. Rev Geophys 35(3): 245-296.
https://doi.org/10.1029/97RG00426

Iverson RM, George DL (2014) A depth-averaged debris-flow model that includes the effects of evolving dilatancy. I. Physical basis. P Roy Soc A-Math Phy 470 (2170): 20130819.
https://doi.org/10.1098/rspa.2013.0819

Jing L, Kwok1 CY, Leung YF, et al. (2018) Runout Scaling and

Deposit Morphology of Rapid Mudflows. J Geophys Res-Earth 123: 2004–2023.
https://doi.org/10.1029/2018JF004667

Johnson AM, Rahn PH (1970) Mobilization of debris flows. Zeitschrift fur Geomorphologie 9 (Suppl): 168- 186.

Kaitna R, Dietrich WE, Hsu L (2014) Surface slopes, velocity profiles and fluid pressure in coarse-grained debris flows saturated with water and mud. J Fluid Mech 741: 377-403.
https://doi.org/10.1017/jfm.2013.675

Lagrée PY, Staron L, Popinet S (2011) The granular column collapse as a continuum: validity of a two-dimensional Navier–Stokes model with a μ(I)-rheology. J Fluid Mech 686: 378-408.
https://doi.org/10.1017/jfm.2011.335

Leonardi A, Wittel FK, Mendoza M, et al. (2016) Particle–fluid–structure interaction for debris flow impact on flexible structures. Comput-Aided Civ Inf 31(5): 323-333.
https://doi.org/10.1111/mice.12165

Li X, Zhao J (2018) Dam-break of mixtures consisting of non-Newtonian liquids and granular particles. Powder Technol 338: 493-505.
https://doi.org/10.1016/j.powtec.2018.07.021

Lin P, Liu PLF (1998) A numerical study of breaking waves in the surf zone. J Fluid Mech 359: 239-264.
https://doi.org/10.1017/S002211209700846X

Lin P, Wu Y, Bai J, et al. (2011) A numerical study of dam-break flow and sediment transport from a quake lake. J Earthq Tsunami 5(05): 401-428.
https://doi.org/10.1142/S1793431111001169

Liu D, You Y, Liu J, et al. (2019) Spatial-temporal distribution of debris flow impact pressure on rigid structure. J Mt Sci-Engl 16(4): 793-805.
https://doi.org/10.1007/s11629-018-5316-4

Liu K, Mei CC (1994) Roll waves on a layer of a muddy fluid flowing down a gentle slope—a Bingham model. Phys Fluids 6(8): 2577-2590.
https://doi.org/10.1063/1.868148

Liu KF, Huang MC (2006) Numerical simulation of debris flow with application on hazard area mapping. Computat Geosci 10(2): 221-240.
https://doi.org/10.1007/s10596-005-9020-4

Louge M, Tuccio, M, Lander E, et al. (1996) Capacitance measurements of the volume fraction and velocity of dielectric solids near a grounded wall. Rev Sci Instrum 67: 1869–1877.
https://doi.org/10.1063/1.1146991

Major JJ, Pierson TC (1992) Debris flow rheology: Experimental analysis of fine-grained slurries. Water Resour Res 28: 841–857.

https://doi.org/10.1029/91WR02834

Mei CC, Liu KF, Yuhi M (2001) Mud flow—slow and fast. Geomorphological fluid mechanics. Springer Berlin Heidelberg: 548-577.
https://doi.org/10.1007/3-540-45670-8_22

Nagl G, Hübl J, Kaitna R (2020) Velocity profiles and basal stresses in natural debris flows. Earth Surf Proc Land 45(8): 1764-1776.
https://doi.org/10.1002/esp.4844

O'Brien JS, Julien PY, Fullerton WT (1993) Two-dimensional water flood and mudflow simulation. J Hydraul Eng 119(2): 244-261.
https://doi.org/10.1061/(ASCE)0733-9429(1993)119:2(244)

Qian N, Wan Z (1986) A critical review of the research on hyperconcentrated flow in China. Intl Res. and Training Ctr. on Erosion and Sedimentation, Beijing.

Tang JB, Hu KH (2018) A debris-flow impact pressure model combining material characteristics and flow dynamic parameters. J Mt Sci-Engl 15(12): 2721-2729.
https://doi.org/10.1007/s11629-018-5114-z

Tiefenbacher F, Kern MA (2004) Experimental devices to determine snow avalanche basal friction and velocity profiles. Cold Reg Sci Technol 38, 17-30.
https://doi.org/10.1016/S0165-232X(03)00060-0

Van der Vorst HA (1992) Bi-CGSTAB: A fast and smoothly converging variant of Bi-CG for the solution of nonsymmetric linear systems. Siam J Sci Comput 13(2): 631-644.
https://doi.org/10.1137/0913035

Wang JS, Ni HG, He YS (2000) Finite-Difference TVD Scheme for Computation of Dam-Break Problems. J Hydraul Eng 126(4): 253-262.
https://doi.org/10.1061/(ASCE)0733-9429(2000)126:4(253)

Wang Y, Zhan Q, Yan B (2014) Debris flow rheology and movement. Hunan Science & Technology press. (In Chinese)

Zhang C, Kirby JT, Shi F, et al. (2021) A two-layer non-hydrostatic landslide model for tsunami generation on irregular bathymetry. 1. Theoretical basis. Ocean Model 159: 101749.
https://doi.org/10.1016/j.ocemod.2020.101749

Zhang C, Kirby JT, Shi F, et al. (2021) A two-layer non-hydrostatic landslide model for tsunami generation on irregular bathymetry. 2. Numerical discretization and model validation. Ocean Model 160: 101769.
https://doi.org/10.1016/j.ocemod.2021.101769

Zou Q, Cui P, He J, et al. (2019) Regional risk assessment of debris flows in China-An HRU-based approach. Geomorphology 340: 84-102.
https://doi.org/10.1016/j.geomorph.2019.04.027